optica

Sub-diffraction discrimination with polarization-resolved two-photon excited fluorescence microscopy

DAVID ARTIGAS,[1,2,*] DAVID MERINO,[1] CHRISTOPH POLZER,[3] AND PABLO LOZA-ALVAREZ[1]

[1]*ICFO-Institut de Ciencies Fotoniques, Barcelona Institute of Sciences and Technology, Av. Carl Friedrich Gauss, 3, 08860 Castelldefels, Barcelona, Spain*
[2]*Department of Signal Theory and Communications, Universitat Politècnica de Catalunya, Jordi Girona 1-3, 08034 Barcelona, Spain*
[3]*University of Applied Sciences Munich, Lothstrasse 34, 80335 Munich, Germany*
Corresponding author: david.artigas@icfo.eu

Imaging molecular structures separated by distances of a few nanometers still represents a complex challenge. Moreover, it is normally restricted to observations on thin (few micrometers) samples. In this work, we rotate the polarization of the excitation beam of two-photon excited fluorescence (TPEF) images to show that fluorescent structures at the molecular scale can be discriminated in a living organism. The polarization rotation generates a modulation of the signal intensity in each pixel of the TPEF images that carry information related to the fluorophore orientation. We analyze the signal modulation in every pixel of the polarization-resolved (PR) TPEF images through a Fourier analysis and generate images for the different Fourier components. Doing that, we show that two fluorophores oriented in different directions can be distinguished. Although by imaging the Fourier components the resolution of the optical system restricts the exact localization of two close molecules, discrimination is still possible even when the molecules are located at sub-diffraction distances. We propose a model that predicts this behavior, and demonstrate it experimentally in the neurons of a living *Caenorhabditis elegans* nematode, where we distinguish the walls of an axon with a diameter below the objective resolution. Since the technique is based in TPEF, the method can be extended to deep tissue imaging and has potential applications in single molecule detection, biological sensors, or super-resolution imaging techniques.   © 2017 Optical Society of America

OCIS codes: (170.3880) Medical and biological imaging; (180.4315) Nonlinear microscopy; (190.4180) Multiphoton processes; (120.2130) Ellipsometry and polarimetry.

https://doi.org/10.1364/OPTICA.4.000911

1. INTRODUCTION

Polarization-resolved (PR) microscopy evaluates the interaction of polarized excitation light with the molecular target. This interaction is related to the molecular-scale organization of the target, revealing structural information, such as molecule orientation, molecular order, or molecular conformational changes, well below the diffraction limit. Consequently, PR microscopy has been proposed as a unique technique to study molecular structures [1]. PR microscopy has been studied for different light–sample interaction mechanisms, including one- [2–4], two- [5,6] and three-photon absorption fluorescence [7], second harmonic generation (SHG) [8–12], sum-frequency generation [13] third harmonic generation [14], or four-wave mixing [15]. PR microscopy has also been combined with fluorescence lifetime imaging [16] and super-resolution techniques, providing an ultimate way to optically image molecular organization and structure [17,18].

Recently, a PR super-resolution technique based on a wide-field fluorescence microscope has been shown to disentangle sub-diffraction structures [19]. This work also shows that the signal modulation produced by rotating the linear polarization of the excitation beam is sharpened by superimposing a depletion laser with an orthogonal polarization. The resulting images are analyzed with a statistics-based algorithm that provides the best set of parameters (fluorophore orientation and emitted intensity) in every region of the sample that fits the actual overall modulation. Although some controversy on the performance of the technique has been addressed, claiming that the PR adds little to the super-resolution capability of the stimulated emission depletion (STED) technique [20], the PR images provide a greater amount of information, which has been used in the past to obtain structural information [1–17]. In addition, it is clear that the extra information can be used to improve an image. Then, the question is what aspect of the image does the PR analysis improve? The present work examines the benefits of pure PR two-photon excited fluorescence (TPEF) microscopy to improve imaging, without the use of any combined technique, such as stimulated

emission depletion. In previous work, we used PR-SHG microscopy [21–23] based on the Fourier analysis on every pixel of the intensity modulation with the incident polarization. Here, we extend that methodology to TPEF imaging. For that, we first perform a numerical analysis based on a non-paraxial, full-vector model, taking into account the depolarization introduced by high numerical aperture objectives [24] and the 3D orientation of the fluorescent molecules, followed by the experimental demonstration in the neuron of a live *Caenorhabditis elegans* nematode.

The Fourier analysis shows a specific intensity modulation when the laser beam is precisely centered between two molecules, which depends on the relative orientation of the molecule. This modulation appears as a clear dark line between the two molecules in the Fourier component images. This results in a new structure-based contrast mechanism capable of distinguishing two differently oriented fluorescent molecules, even when their separation is well below the resolution limit of the system. As a result, two differently oriented molecules can be clearly discriminated, even when adjacent (i.e., the distance between molecules is equal to any set scanning step or equivalently, to the pixel size). Although the dark line can appear between two molecules at sub-diffraction distances, the capability to provide the exact position of the molecules (distance to the dark line) is still limited by the resolution of the system; therefore, super-resolution by localization is, in general, not achieved by plotting the parameters of the Fourier analysis. This sub-diffraction discrimination capability is also present in larger samples with two regions, with fluorophores oriented in well-differentiated directions. In this case, the border between the two regions can be determined with sub-diffraction precision. This concept is experimentally applied in a motor neuron of a living *C. elegans* nematode to distinguish the walls of an axon with a diameter below the objective resolution. The experimental images are analyzed, showing that two possible distributions of the fluorophore orientation are consistent with the results.

2. THEORETICAL AND NUMERICAL FORMALISM

The fluorescence signal collected by an objective in a laser-scanning TPEF microscope, P_I, depends on the transition dipole moment, $\vec{\mu}^{abs}$, the excitation electric field in the focal plane, $\vec{E}^{exc}$, and the electric field radiated by the fluorescent molecule, $\vec{E}^{rad}$, as [1]

$$P_I(\vec{r}\,') \propto N \int_{NA} \int_V \int_\Omega |\vec{\mu}^{abs}(\vec{r}, \Omega) \cdot \vec{E}^{exc}(\vec{r} - \vec{r}\,')|^4 |\vec{E}^{rad}(\vec{r}, \hat{\kappa}, \Omega)|^2$$
$$\times f(\vec{r}, \Omega) \mathrm{d}\Omega \mathrm{d}V \mathrm{d}\hat{\kappa}. \tag{1}$$

Here, N is the density of fluorescent molecules or fluorophores; $\vec{r}$ indicates position in the lab coordinate system, where x and y are parallel to the imaging plane and z is the light propagation axis; and $f(\vec{r}, \Omega)$ describes the distribution of the fluorescent molecules, aligned along a certain direction Ω, in the infinitesimal volume dV. We use modified spherical coordinates to define Ω, where θ is the polar angle measured with respect to the x axis, and ϕ is the azimuthal angle measured with respect to the focal plane [see, Fig. 1(a)]. The dot product $\vec{\mu}^{abs} \cdot \vec{E}^{exc}$ and $f(\vec{r}, \Omega)$ in Eq. (1) results in the absorption probability in each point of the excited volume. Its integration over the whole volume V and orientation Ω is proportional to the absorbed light energy.
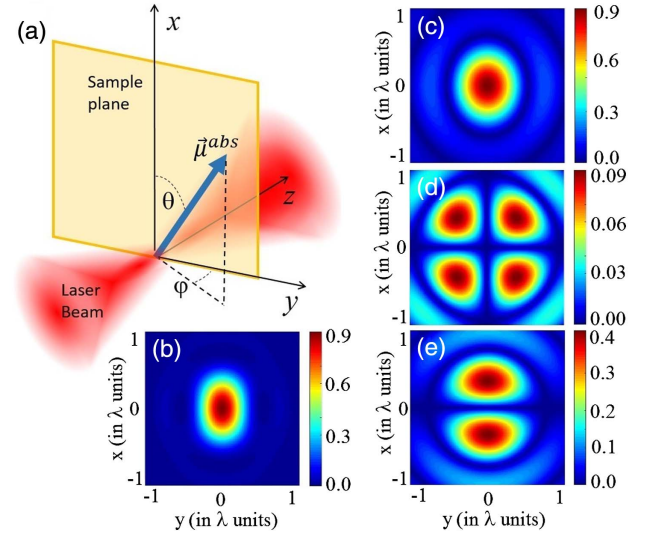

Fig. 1. (a) Coordinate system and angles defining the orientation of the transition dipole moment. (b) Intensity of the electric field at the focal plane of an objective with NA = 1.4. The polarization at the objective back aperture is linear and oriented in the x direction. Local amplitudes for the electric field components are (c) E_x, (d) E_y, and (e) E_z.

The image is generated by the electric field radiated by the fluorescent molecules, $\vec{E}^{rad}$, which can be expressed in terms of the propagation direction $\hat{\kappa}$ as [1]

$$\vec{E}^{rad}(\vec{r}, \hat{\kappa}) \propto \hat{\kappa} \times [\hat{\kappa} \times \vec{\mu}^{em}(\vec{r})], \tag{2}$$

where $\vec{\mu}^{em}$ is the molecular emission dipole of the fluorophore. For simplicity, we consider $\vec{\mu}^{abs} = \vec{\mu}^{em}$, although in general these two magnitudes can differ. In Eq. (1), the integral over all the $\hat{\kappa}$ directions within the objective NA is proportional to the signal measured by the detector. Finally, the scanning of the excitation field $\vec{E}^{exc}$ from point to point within the focal plane is denoted by the scanning coordinate $\vec{r}\,'$.

In a general situation, the fluorophores can be oriented in any direction, forming an angle with the sample plane. Consequently, there is an interaction between the field component E_z and $\vec{\mu}^{abs}$ that cannot be neglected [24,25]. In addition, according to Eq. (2), the main lobe of the radiated field $\vec{E}^{rad}$ is perpendicular to the $\vec{\mu}^{em}$ direction. As a result, the main radiation lobe of molecules oriented out of the plane is not aligned with the objective optical axis, $\hat{z}$. For these two reasons in this work we do not consider the planar wave approximation, a usual approach in PR microscopy [1,11,12,21–23] that assumes, first, a uniform polarization at the focal volume and, second, $\vec{E}^{rad}$ only propagates along the $\hat{z}$ direction. Instead, we take into account the full vector field $\vec{E}^{exc}$ in the whole focal volume as well as all the $\hat{\kappa}$ directions in $\vec{E}^{rad}$ to integrate over the objective NA. To take into account the local polarization in every point of the focal plane of a high NA objective, we use the full vector analytical expressions of $\vec{E}^{exc}$ in Ref. [24]. Figure 1(b) shows the light intensity distribution at the focal plane when the laser beam is polarized along the $\hat{x}$ direction at the objective back aperture. The corresponding local field amplitude is plotted in Figs. 1(c)–1(e) for the E_x, E_y, and E_z components, respectively. Different polarizations with an orientation α, measured with respect to the x (vertical) axis, are considered by rotating the electric field shown in

Figs. 1(c)–1(e). The polarization distribution and the elliptical shape of the intensity at the focus of a high NA objective have been previously used to obtain nanoscale resolution [26].

We create a virtual sample by assigning a molecule with a predominant direction of $\vec{\mu}^{\text{abs}}$ to each discretized volume ΔV. These discretized volumes are chosen to be small so that there is only one molecule in each of them, $N\Delta\vec{r} \approx 1$. We can assume for simplicity that $f(\Omega) = \delta(\Omega - \Omega_i)$, that is, $\vec{\mu}^{\text{abs}}$ in the discretized position $\vec{r}_i$ is oriented along the direction Ω_i. According to this approximation, Eq. (1) can be reduced to

$$P_I(\vec{r}') \propto \sum_{\hat{\kappa}_j} \sum_{\vec{r}_i} |\vec{\mu}^{\text{abs}}(\vec{r}_i) \cdot \vec{E}^{\text{exc}}(\vec{r}_i - \vec{r}'_k)|^4 |\vec{E}^{\text{rad}}(\vec{r}_i, \hat{\kappa}_j)|^2 \Delta V \Delta \hat{\kappa}.$$

(3)

Numerical images of virtual samples are then generated by scanning $\vec{E}^{\text{exc}}$ at the positions $\vec{r}'$ in the focal plane for different orientations of the linearly polarized excitation light, α.

Figure 2 shows images of a single molecule at the center of the field of view for 8 different orientations of the input polarization, using an excitation wavelength, $\lambda = 810$ nm, and a scanning step of 32 nm. Figure 2(a) shows the image when $\vec{\mu}^{\text{abs}}$ is oriented along the vertical $\hat{x}$ direction ($\theta = 0°$). The results show that when changing the polarization, the intensity of the spot decreases, and it starts to take an oval shape. When this polarization approaches $\alpha = 90°$, the effect of the component E_y in Fig. 1(d) starts to predominate, and the spot in the image is split into four lobes. Also, in this case, the fluorescence intensity is reduced more than four orders of magnitude, compared to the first panel at $\alpha = 0°$ (incident field is parallel to $\vec{\mu}^{\text{abs}}$). This corresponds to an intensity typically comparable to the noise level in any experimental
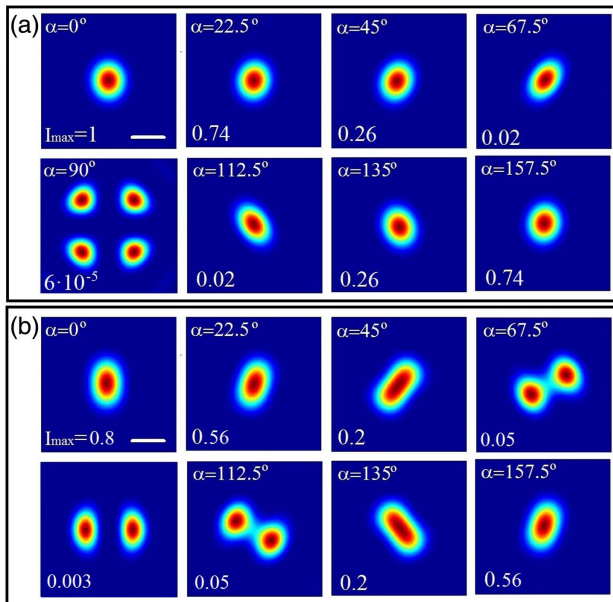
situation, making the observation of this effect very difficult. In the case of Fig. 2(b), where $\vec{\mu}^{\text{abs}}$ is oriented out of the sample plane ($\theta = 45°$, $\phi = 90°$), the existence of the $\hat{z}$ components in $\vec{\mu}^{\text{abs}}$ masks the effect of the E_y component, making the fluorescence response more predominant due to the interaction with the E_z field component [Fig. 1(e)]. Here, the image shows a clear deformation of the spot when the incident polarization is $\alpha > 45°$, which starts to split into two lobes near $\alpha = 60°$. Note that the magnitude of the collected signal at $\alpha = 67.5°$ is not negligible [1–2 orders of magnitude lower than in the first panel in Fig. 2(a)]. Therefore, the effect of the E_z component should not be ignored in a real experiment involving a collection of aligned molecules.

The images in Fig. 2 are examples of how the signal in a pixel can dramatically change, depending on the relative orientation of a molecule, with respect the incident light polarization. The Fourier transform is often used to analyze the change of the signal with respect to a given coordinate (usually time). We decided to analyze the Fourier transform in every pixel with respect to polarization. For that, the N individual images for every polarization obtained from Eq. (3), $P_I(x, y)$, are used to create a 3D image where the third coordinate is the polarization, that is, $P_I(x, y, \alpha)$. The Fourier transform is then applied to the α coordinate, resulting in

$$P_F(x, y, f_p) = \text{FT}\{P_I(x, y, \alpha\}.$$

(4)

The result, $P_F(x, y, f_p)$, corresponds to N images for each Fourier component f_p. The image for the zero Fourier component, $f_p = 0$, provides a measure of the average intensity in every pixel. The first component image, $f_p = 1$, gives information on the intensity modulation with a period of $180°$ along the angle α, while the second component, $f_p = 2$, corresponds to variation with a period of $90°$, and so on. Therefore, the image for every spectral component provides information of the variation of the intensity in every pixel.

3. DISCRIMINATING TWO CLOSE MOLECULES

Here we test the possibility of using the images described above to distinguish two close molecules. For that, we obtain the image for
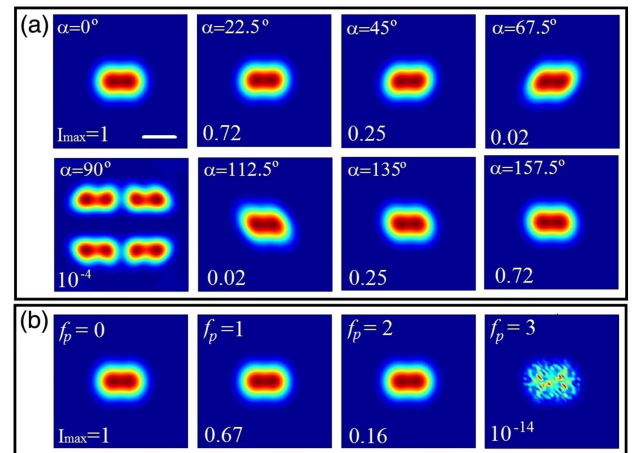

Fig. 2.   (a) Images of a single fluorophore with $\vec{\mu}^{\text{abs}}$ oriented in the x vertical direction ($\theta = 0°$) obtained from Eq. (3) for 8 input polarizations α. (b) Same as (a) but with $\vec{\mu}^{\text{abs}}$ out of plane ($\theta = 45°$, $\phi = 90°$). The normalized values of the maximum intensities are shown in the bottom-left corner in each panel. The normalization was performed with respect to the first panel in (a), where $I_{\text{max}} = 1$. Objective with $NA = 1.4$ and $\lambda = 810$ nm. The scanning step is 32 nm, resulting in $\Delta V = 32$ nm × 32 nm × 32 nm. The scale bar corresponds to 500 nm.

Fig. 3.   (a) PR images corresponding to two molecules at the focal plane. The distance between molecules is $d = 290$ nm, and $\vec{\mu}^{\text{abs}}$ is oriented in the vertical direction ($\theta = 0°$ and $\Delta\theta = 0°$) in both molecules, and (b) PR analysis with the images for the four first Fourier components $f_p = 0, 1, 2,$ and 3. The bar corresponds to 500 nm. Wavelength, NA, and scanning step are the same as Fig. 2.

8 different polarization directions [as shown in Fig. 3(a)] and perform a Fourier transform of the intensity modulation in each pixel using Eq. (4). Figure 3(b) shows the images for the first four Fourier components. In these numerical simulations, high Fourier components with $f_p > 2$ result in noise [right panel in Fig. 3(b)]. We then decided to limit ourselves to analyses of the three first Fourier images, but we cannot dissuade the use of higher Fourier components in other works.

The results in Fig. 3(a) are obtained assuming the same objective and scanning step as in Fig. 1. The distance between molecules is $d = 290$ nm (i.e., at the resolution limit using the Abbe criterion), and $\vec{\mu}^{abs}$ is oriented parallel to the $\hat{x}$ direction in both molecules ($\theta = 0$). Note that the images for the first three Fourier components in Fig. 3(b) are almost identical, and they are equal to the first image in Fig. 3(a) with polarization with $\alpha = 0°$ (aligned along $\vec{\mu}^{abs}$). This is because splitting the focal spot into four lobes at input polarizations $\alpha \approx 90°$ (caused by E_y) does not have an appreciable effect because of the low intensity of the image at that polarization.

A different situation arises when the orientation of $\vec{\mu}^{abs}$ in the two molecules differs by a certain angle. Let us consider an orientation angle with respect the x axis, $\theta = 45°$, for both molecules, but $\phi = 0°$ and $\phi = 180°$ for the right and left molecules, respectively (or equivalently, $\Delta\theta = 90°$). Figure 4(a), left column, shows selected images for different polarization angles α when the distance between molecules is $d = 290$ nm. The images show a fluorescent spot that moves from right to left, depending on whether the electric field is parallel to the momentum of the right or left molecule. As a result, the average modulation around each molecule is identical, and the image for the Fourier component $f_p = 0$ [Fig. 4(a), right column, top] becomes similar to that obtained for the two molecules with parallel $\vec{\mu}^{abs}$ [Fig. 3(b), first panel]. However, the behavior of the Fourier component $f_p = 1$ [Fig. 4(a), right column, middle] is clearly different. Here, the
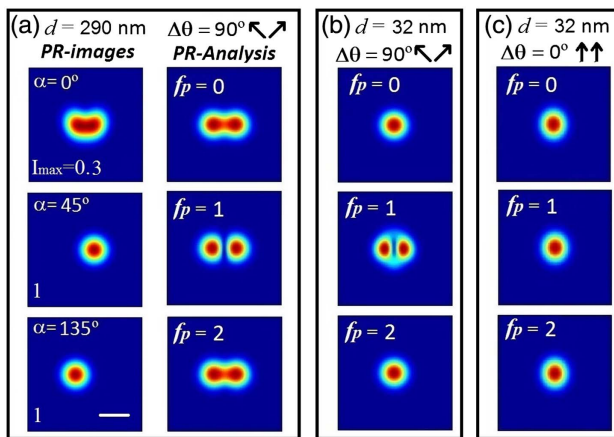
intensity of the pixels at the intermediate points between the two molecules remains almost constant during the lateral displacement of the spot. As a consequence, the Fourier component $f_p = 1$ at these pixels is much lower than that at the pixels near the position of the molecule, resulting in a dark line between the two molecules. Remarkably, this dark line is also appreciable even when the two molecules are adjacent (at nearby pixel, $d = 32$ nm), resulting in an unprecedented capability to discriminate between two molecules with different $\vec{\mu}^{abs}$ [Fig. 4(b)]. This discrimination capacity disappears when $\vec{\mu}^{abs}$ for the two molecules are parallel [see Fig. 4(c)]. Notice, however, that the distance between maxima of the two spots in the Fourier component $f_p = 1$ is 300 nm for a separation of $d = 290$ nm [Fig. 4(a), center] and 255 nm for a separation $d = 32$ nm [Fig. 4(b), center]. This result exemplifies the difference between sub-diffraction discrimination and super-resolution: discrimination of two molecules at sub-diffraction distances ($d = 32$ nm) is possible (the dark line is clearly visible), but the retrieved position of the two molecules in the images appears to be at $d = 255$ nm, implying that localization cannot be achieved beyond the objective resolution (in our examples 290 nm, following the Abbe criterion). Consequently, the use of this analysis should not be related to a super-resolution capability, but rather to a contrast technique that can discriminate between, but not locate, two molecules with different orientations that are separated by a distance smaller than can be resolved by the optical system.

To assess the sub-diffraction discrimination capabilities, we analyze the Fourier components in terms of the difference in orientation between two molecules, $\Delta\theta$, at a distance $d = 32$ nm apart (Fig. 5). Again, the Fourier component at $f_p = 0$ only provides the average intensity and is equivalent for all the values of $\Delta\theta$. The image for the Fourier component $f_p = 1$ is practically constant in the range $0° < \Delta\theta < 75$, but above this value, the lobe in the image starts to split, and the discrimination effect appears in the range $80° < \Delta\theta < 100°$. Similarly, images for the Fourier component $f_p = 2$ show the same discrimination effects at lower values of $\Delta\theta$, in the range $40° < \Delta\theta < 50°$ (and $130° < \Delta\theta < 140°$). In the specific case of $\Delta\theta = 45°$, the maximum intensity is collected for a polarization of the incident light $\alpha = \pm 22.5°$ and the minimum is collected at $\alpha = \mp 67.5°$, that is, when the polarization orientation, α, is parallel or perpendicular to the orientation $\vec{\mu}^{abs}$ of one of the

Fig. 4. (a) PR images (left column) and PR analysis with the images for the three Fourier components $f_p = 0$, 1 and 2 (right column) corresponding to two molecules at the focal plane. The distance between molecules is $d = 290$ nm. The $\vec{\mu}^{abs}$ orientation for the right and left molecule are $\theta = 45°$, $\phi = 0°$ and $\theta = 45°$, $\phi = 180°$, respectively, resulting in $\Delta\theta = 90°$ in both molecules, as shown by the arrows in the top right corner. (b) PR analysis corresponding to case (a) but decreasing the distance between molecules to $d = 32$ nm (one scanning step). (c) Same as (b) but with $\vec{\mu}^{abs}$ oriented parallel to each molecule ($\Delta\theta = 0°$, as shown by the arrows at the top right corner). Wavelength, NA, and scanning step are the same as Fig. 2. The bar corresponds to 500 nm.
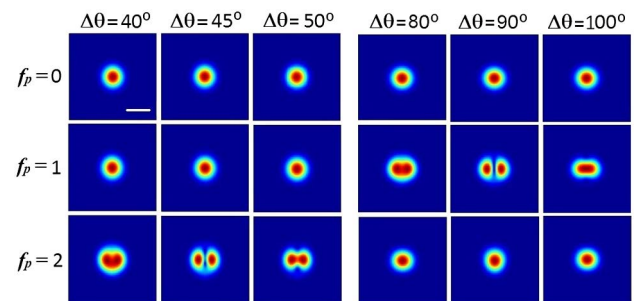

Fig. 5. Images for the Fourier components of two molecules with a separation distance of $d = 32$ nm, with $\vec{\mu}^{abs}$ laying in the focal plane with a different orientation, denoted by the angle $\Delta\theta$. Fourier component images for $\Delta\theta < 35°$ result in a single spot and are not shown. Wavelength, NA, and scanning step are the same than Fig. 2. Bar corresponds to 500 nm.
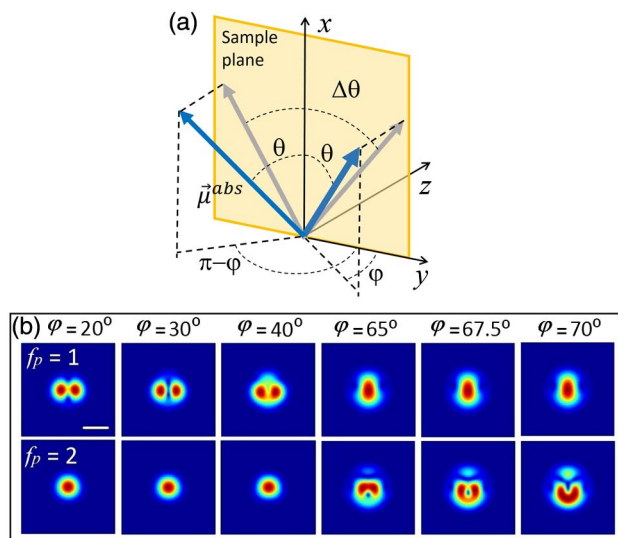
Fig. 6. (a) Lab coordinate system with the definition of the angles for two molecules. $\vec{\mu}^{abs}$ is the plot in blue and the corresponding projection on the sample plane in grey. In this case $\Delta\theta$ indicates the apparent angle between the projected vectors. (b) Images for the Fourier components $f_p = 1$ and 2 for a distance between molecules of $d = 32$ nm and $\theta = 50°$ (initially $\Delta\theta = 100°$), with a changing angle φ (out of the plane). Wavelength, NA, and scanning step are the same as Fig. 2. Bar corresponds to 500 nm.

two molecules. This indicates that the periodicity of the intensity modulation with respect to α is 90°, resulting in a visible discrimination effect in the Fourier component $f_p = 2$.

Until now, we have only considered that both fluorescent molecules are oriented parallel to the sample plane, that is, $\varphi = 0°$ or 180°. Next, we explore the situation when the fluorescent molecules are oriented with directions out of the sample plane. As an example, we consider two molecules, both with $\vec{\mu}^{abs}$ oriented at a fixed angle $\theta = 50°$, but the out of plane angle is changed to a value φ and $\pi - \varphi$ for the right and left molecules, respectively [see lab coordinates in Fig. 6(a)]. In this configuration, the difference in angles between molecules is $\Delta\theta = 100°$ when $\varphi = 0$. Then, as φ increases, the projection of $\vec{\mu}^{abs}$ in the x–y plane [grey arrows in Fig. 6(a)] results in an apparent narrower angle $\Delta\theta$ and, similarly to Fig. 5, the discrimination improves, with a maximum at $\varphi = 30°$ [see first row in Fig. 6(b)]. As the value of φ increases, the apparent (projection) value of $\Delta\theta$ is reduced, and as the projected angle $\Delta\theta$ reaches 45°, the discrimination effect should appear in the Fourier component $f_p = 2$. However, the discrimination is clearly ruined by the interaction of the field component E_z with the z-component of $\vec{\mu}^{abs}$, as the second row in Fig. 6(b) shows. If initial values of $\theta > 60°$ are considered, an apparent (projected) angle of $\Delta\theta = 90°$ requires higher angles, φ, which increases the $\vec{\mu}_z^{abs}$-component, and the discrimination is also spoiled for $f_p = 1$.

4. EXTREME CONTRAST IMAGING IN LARGE SAMPLES: EXPERIMENTAL AND NUMERICAL RESULTS

The epi-detection TPEF microscopy setup was based on an adapted inverted microscope (TE2000-U, Nikon) and a pair of galvanometric mirrors (Cambridge Technology). The excitation source was a Ti:sapphire laser (MIRA 900f, Coherent), operating at a central wavelength of 810 nm. After the galvanometric scanning mirrors, we placed a linear polarizer (ThorLabs, LPNIR050) parallel to the incoming laser linear polarization and a zero order $\lambda/2$ wave plate (QWPO-810, CVI Melles Griot) on a motorized rotational stage (AG-PR100, Newport Corporation), which was rotated in steps to change the polarization at the sample plane. A telescope arrangement was used to fill the back aperture of the objective lens. The objective was $60 \times$, $(NA) = 1.4$, (PlanApo, Nikon). The microscope mounted a long-wave-pass dichroic beam splitter (FF665, Semrock Inc), a BG39 filter, and a PMT (H9305-04, Hamamatsu). The polarization of the laser source has a typical extinction ratio value of $>500:1$. The average extinction ratios for all those used (nine) polarizations were $63 \pm 3:1$ after the dichroic mirror and $25 \pm 2:1$ after the $1.4NA$ objective. The differences in power for each polarization were lower than 5%. A labVIEW interface program controlled the raster scanning of the galvo-mirrors and the data acquisition (DAQ) card. The typical frame acquisition time for a single 500×500 pixels image was ~1 s, the pixel size (scanning step) was 72 nm, and the field of view was 37×37 μm. Images were acquired for 9 different rotating polarizations. The process was repeated 4 times, acquiring 4 images for each polarization. A MATLAB program was used to average the images for each polarization, reducing noise, and to perform the PR analysis. In total, acquisition and image processing time was around 1 min.

We used living *C. elegans* nematodes (strain juIs76 [unc-25:: gfp] II) to experimentally demonstrate extreme contrast in a real sample. The samples were maintained using methods reported elsewhere [27]. Adult hermaphrodite specimens were mounted between two 40-μm glass slides on a 2% agar pad with 0.8 μl of 25 mM NaN₃ as anesthesia, which immobilized the worms and reduced motion artifacts. The mounts were sealed with melted paraffin. Imaging was performed for a period of less than half an hour to guarantee worm viability. The laboratory temperature was 21°C. This worm strain expresses green fluorescent protein (GFP) in a specific set of neurons.

The axons in the worm have a cylindrical geometry with a typical diameter of 100–200 nm [28]. The fluorescent proteins are assumed to be attached to the outer membrane (axolemma). Accordingly, the central part of the axon acts as a symmetry axis for fluorophore orientation, forming a highly ordered collection of fluorescent molecules. PR analysis can thus, in principle, discriminate two oppositely placed fluorescent molecules on the walls in the axon (i.e., placed on each side of the symmetry axis) only when the molecules present an angle difference $\Delta\theta$. Figure 7(a) shows a typical TPEF image at a given polarization, and Visualization 1 shows the change in fluorescence intensity in the axons due to a change in the excitation polarization direction. Note that TPEF images do not show, by themselves, any structure within the axons. The Fourier components obtained by analyzing the intensity modulation in each pixel using the 9 images in the video are shown in Figs. 7(b)–7(d). As expected, the component for $f_p = 0$ is equivalent to the average of the images for every polarization, resembling Fig. 7(a) with a single polarization. Remarkably, even taking into account that the diameter of the axon is below the resolution of the optical system, the discrimination effect is apparent on the images for both the $f_p = 1$ [Fig. 7(c)] and $f_p = 2$ [Fig. 7(d)] Fourier components. We
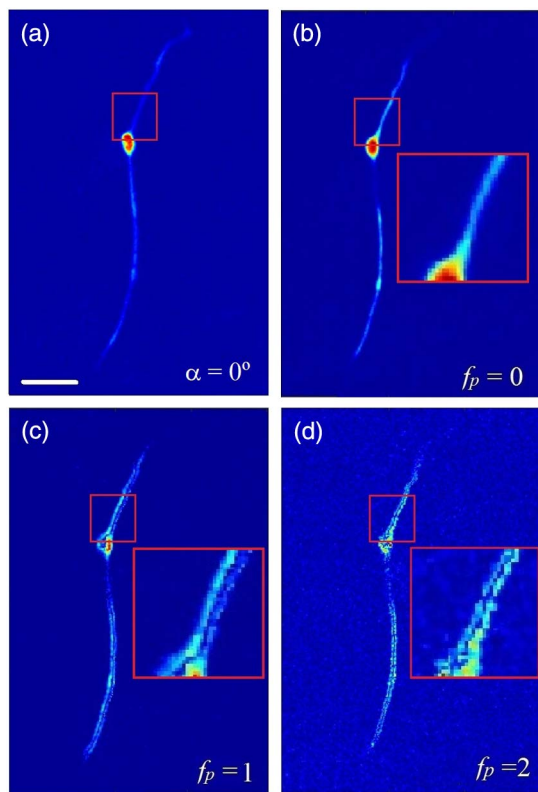
Fig. 7. (a) Image of a neuron in a living *C. elegans* nematode using a single polarization, in this case, in the vertical direction (0°). Visualization 1 shows the images for the 9 polarizations α. Images for the Fourier components, (b) $f_p = 0$, (c) $f_p = 1$, and (d) $f_p = 2$, are calculated from the experimental images in the Supplementary Video. The insets show a 3×magnification of the area with the red square. Bar corresponds to 5 µm.
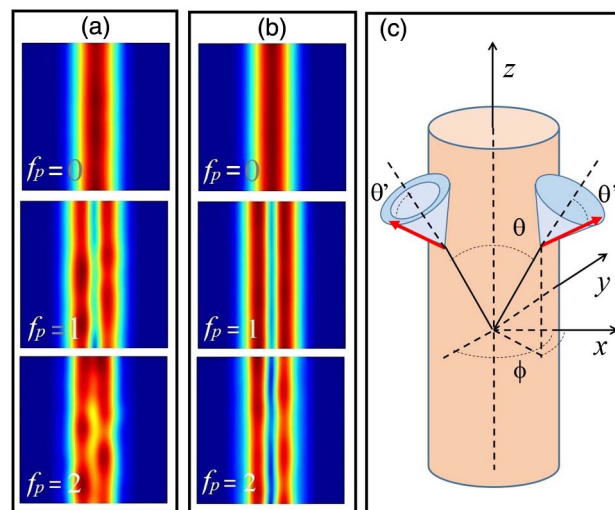

Fig. 8. Numerical images synthesized for two possible probability distributions: (a) conical constant-filled distribution centered at $\theta = 60°$ and conus aperture $\theta' = 20° \pm 5°$; (b) conical empty distribution centered at $\theta = 62°$ with an internal conus aperture (inner wall) of $\theta' = 14° \pm 2°$ and an external conus aperture (outer wall) of $\theta' = 20° \pm 2°$. (c) Scheme of the lab coordinate system, with the axon wall (light brown cylinder) and two conical distributions: filled and empty blue conus on the right and left side of the cylinder, respectively.

repeated the experiment for different neurons and determined that noise largely affected the results. This was particularly an issue for the $f_p = 2$ Fourier component, which, in some cases with moderate noise, was more difficult to generate than the $f_p = 1$ Fourier component. Finally, the Fourier component images of the soma show a certain pattern. However, the meaning of the pattern in the soma is unclear, as the images changed from sample to sample, which may indicate a low order in the GFP orientation.

These results, in addition to experimentally demonstrating sub-diffraction discrimination, can be used to predict the dipole orientation distribution $f(\Omega)$ of the fluorescent molecule. The fact that discrimination appears for both Fourier components cannot be explained by considering a fixed and identical orientation of the fluorescent molecule on all surfaces of the axon. Under these conditions, discrimination would appear only in the $f_p = 1$ or $f_p = 2$ Fourier component, depending on the $\vec{\mu}^{abs}$ orientation, as explained in Fig. 5. Therefore, to replicate the experimental results, we considered an orientation distribution $f(\Omega)$ in the numerical method. For that, the sampling in the numerical method is reduced to a volume of $\Delta V = 8 \times 8 \times 8 \text{ nm}^3$, and different orientations of the molecule are assigned to every ΔV, following different probability distributions $f(\Omega)$.

According to the results in Section 3, the discrimination observed in the images for $f_p = 1$ and $f_p = 2$ in Figs. 7(c) and 7(d), respectively, requires a similar number of fluorophores with $\vec{\mu}^{abs}$ oriented at an angle of $\theta = 45°$ and 22.5° (or 67.5°),

respectively. These orientations were taken as starting points to assay different distribution solutions for $f(\Omega)$. After different trials, we came up with two possible solutions of $f(\Omega)$ that approximately reproduced the experimental results. The first situation corresponds to a conical constant (filled) distribution with a conus centered at $\theta = 60°$ and an aperture of $\theta' = 20° \pm 5°$. The numerical images of the Fourier components generated with this distribution are shown in Fig. 8(a). The second distribution, resulting in the images in Fig. 8(b), is an empty conical distribution, with the cone centered at $\theta = 62°$ (no fluorophores in this direction), an internal conus aperture (inner wall) of $\theta' = 14° \pm 2°$, and an external conus aperture (outer wall) of $\theta' = 20° \pm 2°$. Figure 8(c) shows a scheme of the two possible distributions. Note that both distributions have an important dipole orientation density near $\theta = 45°$ (corresponding to a difference in orientation between opposite walls of $\Delta\theta \approx 90°$) that results in the discrimination shown for the $f_p = 1$ Fourier component. Discrimination in the image of the Fourier component $f_p = 2$ is provided by the existence of molecules with $\vec{\mu}^{abs}$ oriented in the range 70°–80° ($\Delta\theta \approx 140°$–160°). We checked that the existence of fluorophores with $\theta < 25°$ in the two distributions reduces the existence of extreme contrast in both the images of the $f_p = 1$ and $f_p = 2$ Fourier components. Finally, the cylindrical geometry of the axon results in a large number of fluorophores oriented out of the plane, and the loss of discrimination described in Fig. 6 is important, reducing the contribution to the image of fluorophores located on the top or the bottom of the axon cylindrical surface.

This retrieved orientation can be related with the actual orientation of the GFP in the axon. The GFP structure consists of an eleven-stranded β-sheet cylinder that unfolds at the center to form the *p*-hydroxybenzylideneimidazolinone fluorophore. The fluorophore shows planar geometry, with the normal of this plane at an

angle of ∼30° with respect to the cylinder axis. This results in an orientation of the fluorophore of ∼60°, with respect the axis of the β-sheet cylinder [29,30]. This angle coincides with the central angle for the two retrieved orientation distributions. This indicates that the GFP cylinder is mainly oriented parallel to the axon axis, with the fluorophore pointing outwards.

5. DISCUSSION AND CONCLUSIONS

In this work, we theoretically and experimentally show that the Fourier analysis of images obtained with a PR TPEF microscope can be used to discriminate two fluorophores at distances below the diffraction limit. This is based on acquiring a set of images from different excitation beam polarizations, performing the Fourier transform in every pixel, in terms of the polarization orientation, and imaging the Fourier components. Sub-diffraction discrimination is observed when the orientation of the fluorophore transition dipole momentum, $\vec{\mu}^{abs}$, is different in two molecules or regions at distances as small as the scanning step. The first Fourier component $f_p = 0$ is only related to the averaged intensity in each pixel at different polarizations; therefore, it does not provide discrimination information. Depending on the orientation difference, $\Delta\theta$, of $\vec{\mu}^{abs}$ within the focal plane, the $f_p = 1$ or $f_p = 2$ Fourier components can be used to discriminate between fluorophores with different orientations. Discrimination in the $f_p = 1$ and $f_p = 2$ components appears when $\Delta\theta \approx 90°$ and $\Delta\theta \approx 45°$ (or 135°), respectively, and decreases when the fluorophores are oriented out of the focal plane. Molecules oriented with other values of $\Delta\theta$ may show discrimination at higher Fourier components. This imaging analysis can be used in single molecule co-localization experiments to discriminate molecules at a distance below the optical system resolution under high SNR conditions. This can be especially important in the use of Förster resonance energy transfer (FRET) [31], as FRET strongly depends on the orientation of the transition dipole moments of the donor and acceptor fluorophores [32].

In large specimens, where regions of fluorophores aligned with different orientations are considered, discrimination is closely related to the fluorophore orientation distribution, $f(\Omega)$. Here, we have shown how this approach can be used to disentangle sub-diffraction structures in a cell of a living organism. In particular, we have discriminated fluorescent molecular structures sitting on the two opposite walls of an axon in a living *C. elegans* worm. In addition, we have numerically estimated two possible fluorophore distributions on the axon surface, reproducing the experimental results. Here, the discrimination capability is possible because of the high degree of order in the orientation of the fluorophores on the sample.

Given the advantages of TPEF imaging, such as lower absorption and scattering, the technique can be used on living organisms and also deep inside tissue, making it possible to discriminate between molecules in thick specimens.

In conclusion, this technique has potential direct applications in single molecule co-localization experiments to discriminate between molecules at a distance below the optical resolution of biological sensors, increase contrast at the nanometer scale of polarization images, or explain increased image quality in super-resolution techniques based on PR microscopy [18–20].

REFERENCES

1. S. Brasselet, "Polarization-resolved nonlinear microscopy: application to structural molecular and biological imaging," Adv. Opt. Photon. **3**, 205–271 (2011).
2. D. Axelrod, "Carbocyanine dye orientation in red-cell membrane studied by microscopic fluorescence polarization," Biophys. J. **26**, 557–573 (1979).
3. A. M. Vrabioiu and T. J. Mitchison, "Structural insights into yeast septin organization from polarized fluorescence microscopy," Nature **443**, 466–469 (2006).
4. A. Kress, X. Wang, H. Ranchon, J. Savatier, H. Rigneault, P. Ferrand, and S. Brasselet, "Mapping the local organization of cell membranes using excitation-polarization-resolved confocal fluorescence microscopy," Biophys. J. **105**, 127–136 (2013).
5. A. Gasecka, T.-J. Han, C. Favard, B. R. Cho, and S. Brasselet, "Quantitative imaging of molecular order in lipid membranes using two-photon fluorescence polarimetry," Biophys. J. **97**, 2854–2862 (2009).
6. J. Lazar, A. Bondar, S. Timr, and S. J. Firestein, "Two-photon polarization microscopy reveals protein structure and function," Nat. Methods. **8**, 684–690 (2011).
7. A. Gasecka, P. Tauc, A. Bentley, and S. Brasselet, "Investigation of molecular and protein crystals by three photon polarization resolved microscopy," Phys. Rev. Lett. **108**, 263901 (2012).
8. P. Stoller, B. M. Kim, A. M. Rubenchik, K. M. Reiser, and L. B. Da Silva, "Polarization-dependent optical second harmonic imaging of a rat-tail tendon," J. Biomed. Opt. **7**, 205–214 (2000).
9. F. Tiaho, G. Recher, and D. Rouede, "Estimation of helical angles of myosin and collagen by second harmonic generation imaging microscopy," Opt. Express **15**, 12286–12295 (2007).
10. D. Aït-Belkacem, M. Guilbert, M. Roche, J. Duboisset, P. Ferrand, G. Sockalingum, P. Jeannesson, and S. Brasselet, "Microscopic structural study of collagen aging in isolated fibrils using polarized second harmonic generation," J. Biomed. Opt. **17**, 080506 (2012).
11. S. Psilodimitrakopoulos, I. Amat-Roldan, P. Loza-Alvarez, and D. Artigas, "Effect of molecular organization on the image histograms of polarization SHG microscopy," Biomed. Opt. Express **3**, 2681–2693 (2012).
12. S. Psilodimitrakopoulos, P. Loza-Alvarez, and D. Artigas, "Fast monitoring of in-vivo conformational changes in myosin using single scan polarization-SHG microscopy," Biomed. Opt. Express **5**, 4362–4373 (2014).
13. Y. Han, V. Raghunathan, R.-R. Feng, H. Maekawa, C.-Y. Chung, Y. Feng, E. O. Potma, and N.-H. Ge, "Mapping molecular orientation with phase sensitive vibrationally resonant sum-frequency generation microscopy," J. Phys. Chem. B **117**, 6149–6156 (2013).
14. M. Zimmerley, P. Mahou, D. Débarre, M.-C. Schanne-Klein, and E. Beaurepaire, "Probing ordered lipid assemblies with polarized third-harmonic-generation microscopy," Phys. Rev. X **3**, 011002 (2013).
15. H. B. de Aguiar, P. Gasecka, and S. Brasselet, "Quantitative analysis of light scattering in polarization-resolved nonlinear microscopy," Opt. Express **23**, 8960–8973 (2015).
16. J. A. Levitt, D. R. Matthews, S. M. Ameer-Beg, and K. S. Suhling, "Fluorescence lifetime and polarization-resolved imaging in cell biology," Curr. Opin. Biotechnol. **20**, 28–36 (2009).
17. T. Ha, T. A. Laurence, D. S. Chemla, and S. Weiss, "Polarization spectroscopy of single fluorescent molecules," J. Phys. Chem. B **103**, 6839–6850 (1999).
18. C. A. V. Cruz, H. A. Shabana, A. Kressa, N. Bertauxa, S. Monnereta, M. Mavrakisa, J. Savatiera, and S. Brasselet, "Quantitative nanoscale imaging of orientational order in biological filaments by polarized superresolution microscopy," Proc. Natl. Acad. Sci. USA **113**, E820–E828 (2016).

19. N. Hafi, M. Grunwald, L. S. van den Heuvel, T. Aspelmeier, J. Chen, M. Zagrebelsky, O. M. Schütte, C. Steinem, M. Korte, A. Munk, and P. J. Walla, "Fluorescence nanoscopy by polarization modulation and polarization angle narrowing," Nat. Methods **11**, 579–584 (2014).

20. L. Frahm and J. Keller, "Polarization modulation adds little additional information to super-resolution fluorescence microscopy," Nat. Methods **13**, 7–8 (2016).

21. S. Psilodimitrakopoulos, S. I. C. O. Santos, I. Amat-Roldan, A. K. N. Thayil, D. Artigas, and P. Loza-Alvarez, "*In vivo*, pixel-resolution mapping of thick filaments' orientation in nonfibrilar muscle using polarization-sensitive second harmonic generation microscopy," J. Biomed. Opt. **14**, 014001 (2009).

22. S. Psilodimitrakopoulos, D. Artigas, G. Soria, I. Amat-Roldan, A. M. Planas, and P. Loza-Alvarez, "Quantitative discrimination between endogenous SHG sources in mammalian tissue, based on their polarization response," Opt. Express **17**, 10168–10176 (2009).

23. I. Amat-Roldan, S. Psilodimitrakopoulos, P. Loza-Alvarez, and D. Artigas, "Fast image analysis in polarization SHG microscopy," Opt. Express **18**, 17209–17219 (2010).

24. B. Richards and E. Wolf, "Electromagnetic diffraction in optical systems. II. Structure of the image field in an aplanatic system," Proc. R. Soc. London A **253**, 358–379 (1959).

25. E. Yew and C. Sheppard, "Effects of axial field components on second harmonic generation microscopy," Opt. Express **14**, 1167–1174 (2006).

26. K. A. Serrels, E. Ramsay, R. J. Warburton, and D. T. Reid, "Nanoscale optical microscopy in the vectorial focusing regime," Nat. Photonics **2**, 311–314 (2008).

27. S. Brenner, "The genetics of Caenorhabditis elegans," Genetics **77**, 71–94 (1974).

28. http://www.wormatlas.org/hermaphrodite/nervous/Neuroframeset.html.

29. S. Inoue, O. Shimomura, M. Goda, M. Shribak, and P. T. Tran, "Fluorescence polarization of green fluorescence protein," Proc. Natl. Acad. Sci. USA **99**, 4272–4277 (2002).

30. F. I. Rosell and S. G. Boxer, "Polarized absorption spectra of green fluorescent protein single crystals: transition dipole moment directions," Biochemistry **42**, 177–183 (2003).

31. L. Stryer, "Fluorescence energy transfer as a spectroscopic ruler," Annu. Rev. Biochem. **47**, 819–846 (1978).

32. T. Ansbacher, H. K. Srivastava, T. Stein, R. Baer, M. Merkxc, and A. Shurkiz, "Calculation of transition dipole moment in fluorescent proteins—towards efficient energy transfer," Phys. Chem. Chem. Phys. **14**, 4109–4117 (2012).